Reproduction of Rebar Mesh Arrangement Inside Concrete Bridge Deck from Ground Penetrating Radar Volume Images by 3D DFT

Tsukasa Mizutani and Takanori Imai

***Abstract*—Aging of infrastructures has been a worldwide issue, and cost saving by shifting to preventive maintenance is urgent. Especially, damage detection of concrete bridge decks is one of the most important subjects, because of the significant repair costs due to its complicated structure. Rebars are the fundamental components of bridge decks, and they often become the trigger of bridge decks' damages. Previous researches have been focused on detecting the locations of rebars in cross section images acquired by single-channel ground penetrating radar (GPR), however, no research has reproduced 3D rebar mesh arrangement from radar volume images acquired by multi-channel GPR. This paper proposes a method that reproduces 3D rebar mesh that contains the data of vertex location and reflection time from radar volume images. Real scale bridge deck specimens were created in this study and reflections of electromagnetic waves were observed utilizing an on-vehicle GPR. In the proposed method, 3D filtering based on the 3D DFT theory for the noise reduction was applied. Also, automation in detection of the rebar depth was achieved focusing on edges of the images. As a result, 3D rebar meshes were successfully reproduced with appropriate distribution rebar spacing. Also, the method was applied to radar data acquired from a bridge in service. The proposed method effectively functioned for in-service bridge data, and automatically reproduced the mesh of $21\,\mathrm{m}$ length.**

***Index Terms*—Ground penetrating radar (GPR), multi-channel, 3D rebar mesh reproduction, image processing, 3D DFT, radar volume image.**

I. Introduction: Need for Non-Destructive Rebar Detection of Bridge Decks by On-Vehicle GPR

INFRASTRUCTURES in developed countries are rapidly aging. In Japan, maintenance and renewal costs will be about 300 trillion yen over the next 30 years [1]. It is estimated that the cost can be reduced by 100 trillion yen by shifting to preventive maintenance that detects damage in advance and extends the service life of structures. There is an urgent need to develop damage detection technology and to improve the efficiency of maintenance and management through its automation. Damage detection of concrete bridge decks is one of the most important issues, because of the significant repair costs due to its complicated structure. However, the practical damage detection method of bridge decks has not been established yet, and the inspection is currently carried out manually by visual and sound inspection shaving off the asphalt pavement. These inspections are time and money-consuming for all stakeholders, including the national government, local governments and management companies.

Tsukasa Mizutani and Takanori Imai are with the Institute of Industrial Science, the University of Tokyo, Tokyo 153-8505, Japan (e-mail: mizu-t@iis.u-tokyo.ac.jp; t-imai@iis.u-tokyo.ac.jp).

Ground penetrating radar (GPR) is a non-destructive, non-contact, and high-speed measurement technology to obtain information under the ground and structures by emitting electromagnetic waves and observing the reflected waves. There are two main types of GPR: the ground-coupled type that put the antenna as close to the ground as possible, and the air-coupled type that measures the object at a distance from the ground. As the ground-coupled type is closer to the object, it produces less noise and provides a clearer and deeper image. On the contrary, the air-coupled radar can be mounted on a vehicle and it enables high-speed data acquisition. For example, our study utilizes the radar system that can travel at $80\,\mathrm{km/h}$ and acquire the data simultaneously. Especially for the huge number of road infrastructures, it is desired that the air-coupled radar can acquire data at high-speed and analyze the underground in real time.

As specific applications, in the roads other than the bridges, the detection of buried pipes and cavities has been studied [2]–[5]. In the bridge sections, which is the target of this research, damage map generation for the bridge decks [6]–[8] and detection of rebar responses [9]–[13] have been carried out. The detection of rebars is important because it is one of the most fundamental structural component of the bridges. For bridges that design drawings do not exist because of their old age, structural information such as rebar spacing can provide us with the information for determining the need for strengthening. Another point of view is that corrosion of the rebars is the major trigger of the damages of the bridge decks represented by concrete segregation. Identification of the rebar locations in the radar image and detailed analysis of the intensity distribution would contribute to the early detection of various damages.

It is known that the targets such as rebars and buried pipes that can be regarded as point-like objects when seen in a minor axis cross section, appears as hyperbolic responses in radar images [14]–[16]. This is because the antenna's beam has directivity with some width, and electromagnetic waves traveling in oblique direction are reflected and observed. The detection of the rebar responses focusing on this hyperbolic response is currently the mainstream. Specifically, methods to maximize the sum of the squared error between the ideal hyperbolic template and the radar image [7], and methods to detect hyperbolic responses using AdaBoost and the Single Shot Detector object detection model [10], [13] have been

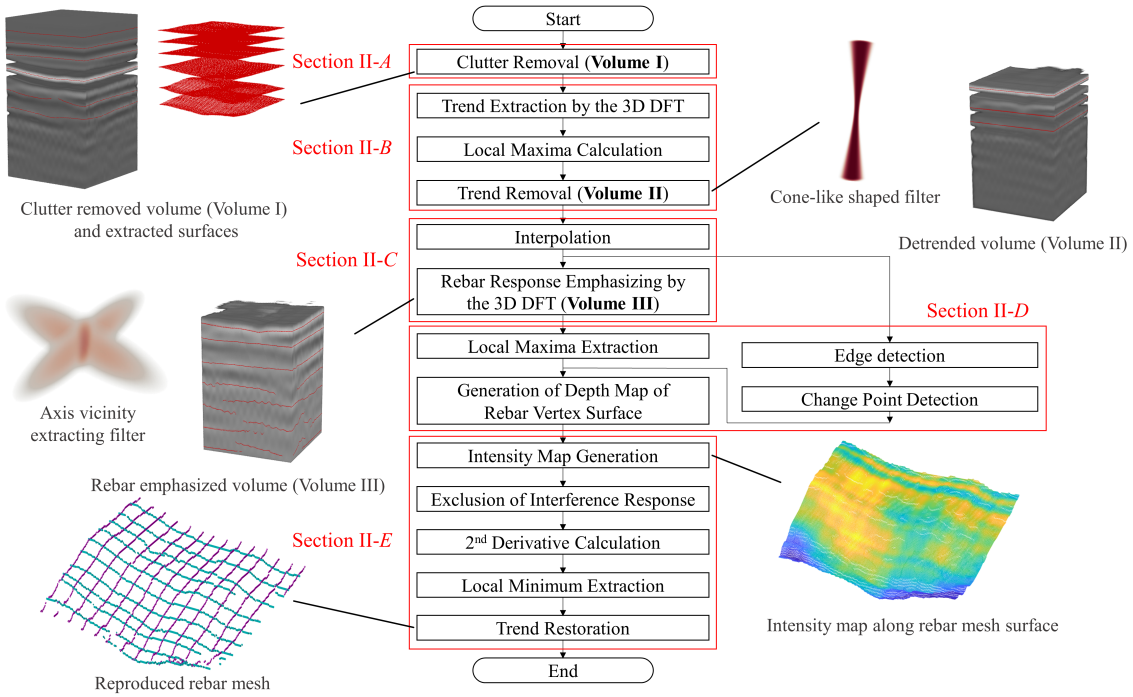

Fig. 1. Flow Chart of the Proposed Algorithm. There are mainly 5 steps; the red squares show the sections that the processing is explained in detail.

proposed. However, most of these methods are applicable to data acquired by ground-coupled radar. This is because the air-coupled radar does not provide isolated hyperbolic responses of densely located objects, due to the larger distance between the antenna and the object resulting in wide hyperbolic shapes overlapping with each others. Because of this phenomena, rebar reflections are recorded as complicated images. In addition, previous studies have mainly focused on cross section images of depth and longitudinal direction cross section image; not so much research have dealt with radar volume images that contains rich spatial information of rebars.

The objective of this study is to reproduce 3D rebar mesh that contains the data of location and reflection time from radar volume images. Especially, we will focus on detecting the vertices of the hyperbolic responses. Rebars are generally placed in a certain spacing. Therefore, focusing on the periodicity of the rebar mesh in the frequency domain by 3D filtering is effective for extracting and enhancing the rebar mesh response. In addition, 3D processing gives us consistent interpretation of the volume images, which is also the strength. The composition of this study is as follows. In Section II, measurements are conducted using real scale bridge deck specimens with two types of rebar spacing. There will be specific explanations of the rebar mesh reproduction algorithm following the flow chart (Figure 1). Also, the verification is done here by comparing the reproduced rebar meshes with design drawings. In Section III, rebar mesh reproduction is performed on in-service bridge data to verify the applicability of the method.

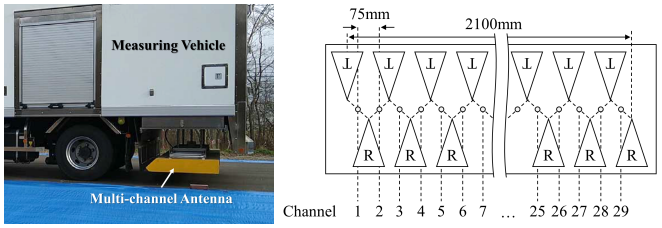

Fig. 2. (a) The utilized vehicle and the GPR antenna installed. (b) Layout of GPR antenna elements.

II. Measurements with Real Scale Bridge Deck Specimens

Measurements were conducted in the test field constructed in Hokkaido, Japan (Figure 2). The results of applying the method to two different rebar spacing are compared in this section. The specimens have main rebars (longitudinal direction) at both 15 cm intervals and distribution rebars (transverse direction) at 15 cm and 30 cm intervals each (Figures 3, 4). They are called as Specimen I and Specimen II in this paper. It should be noted that Specimen II contains some repair marks on the bridge deck. The thickness of the asphalt pavement is 7.5 cm. The processing is done for a volume image that has a length of 200 cm in the longitudinal direction and a width of 210 cm in the transverse direction, and this analysis range is also drawn in Figure 4. The method is divided into five major stages: *A.* pre-processing of the data, *B.* low frequency trend removal, *C.* rebar response enhancement by 3D filtering, *D.* rebar depth estimation, and *E.* rebar mesh reproduction. The processing will be specifically explained in each section.

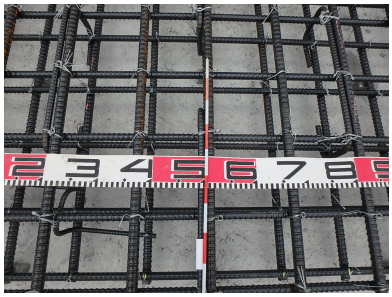

Fig. 3. Rebars inside Specimen I.

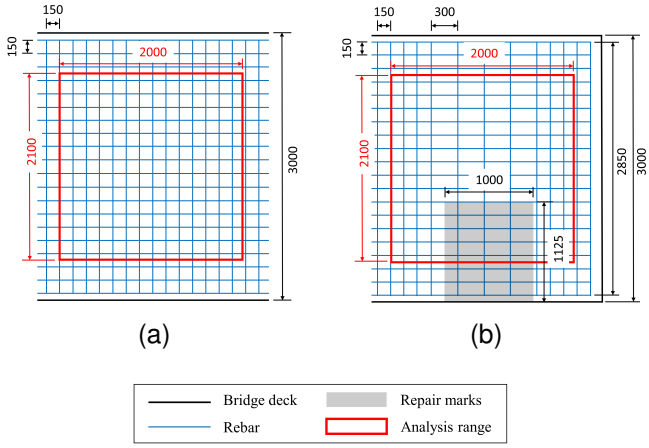

Fig. 4. Rebar arrangements of the bridge deck specimens.(a) Specimen I: Both rebar spacings are 15 cm. (b) Specimen II: Main rebar spacing is at 15 cm and distribution rebar spacing is at 30 cm.

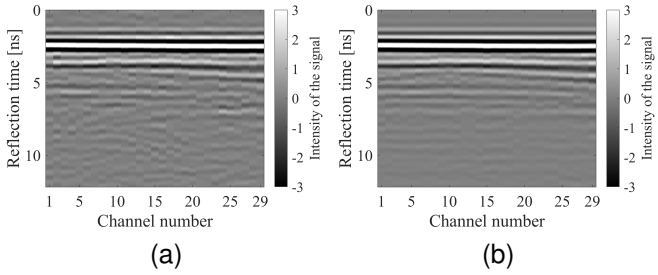

Fig. 5. Changes in channel-depth cross section by clutter removal processing. (a) Image with frequency of 470 to 3030 MHz. (b) Image after clutter removal processing.

A. Pre-processing by Frequency Band Limitation and Zero Offset Removal

In this study, an on-vehicle air-coupled GPR is used: 29 channels are installed at 7.5 cm spacing in the transverse direction (Figure 2b). Section II deal with the data acquired at 1 cm spacing in the longitudinal direction. Electromagnetic waves are transmitted and received by the Stepped-Frequency Continuous Wave (SF-CW) method [17] at bandwidth of 50 to 3030 MHz, interval of 20 MHz. The low-frequency component is noisy due to the low intensity of the transmitted electromagnetic wave due to the antenna characteristics, so only the components above 470 MHz is used. The number

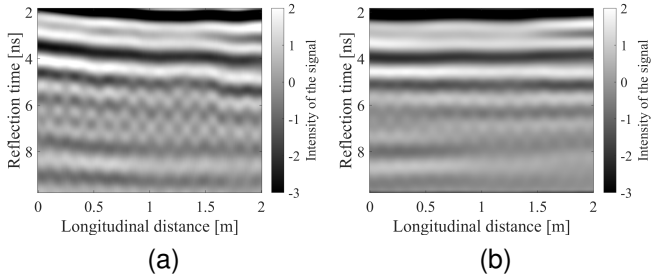

Fig. 6. Comparison of cross section of volume images before and after filtering processing. (a) Cross section of Volume I. (b) Cross section of Volume III, after applying two 3D filters.

of data points was increased to 4096 by zero padding when converting to the time domain to improve the time domain resolution of the signal.

Radar data often contain clutter, which is unwanted reflection waves from objects other than the target objects. The influence of the clutter is especially remarkable in transverse direction that uses multiple antennas that have slightly different frequency characteristics. Background removal is the method to remove clutter or stable signals from the original radar signal [15], [16], [18]. In this study, we applied zero offset removal to each channel; the mean components in the distance direction were subtracted. On the other hand, the mean components in the longitudinal direction includes some significant components such as reflections from the road surface and the rebars. To prevent them from being removed, the mean components of the longitudinal direction from the obtained signal were subtracted and its transverse direction mean value was added again. This can remove only the high frequency components of the clutter. The images before and after processing are shown in Figure 5. We can confirm that overall noise reduction in the transverse direction has been achieved.

B. Low-Frequency Trend Removal by 3D Filtering

Due to the distance from the ground, data acquired by air-coupled GPR gives us unclear hyperbolic responses and contain much noise (Figure 6). 3D filtering is one of the possible solutions that can reduce noise and emphasize the signals' periodicity. However, another problem is that data acquired by an on-vehicle GPR is affected by the vibration of the vehicle and the inhomogeneous permittivity distribution of asphalt and concrete that causes undulation in the depth direction. Because of this effect, reflections from asphalt pavement, bridge deck surface, and rebars are seen as trended curved surfaces in radar volume images, even if they are almost flat in real. When the 3D DFT is performed to this volume with a trend, the rebar response components appear off-axis in the frequency domain (Appendix), and it becomes difficult to perform appropriate filtering that can emphasize the rebar responses in Section II-C. Therefore, in this section, we use the 3D filtering processing to obtain curved surfaces in the radar volume image, and resample the signals in the time domain so that these surfaces become flat.

The 3D filtering is done by first applying the 3D DFT to a volume image, then multiply a filter, and performing the 3D IDFT to the filtered frequency data. Appendix shows that the cone-like shaped filter is effective for extracting the responses of surfaces. Cross sections of the filter is shown in Figure 7a. For strict cone shape being unable to extract the components near the origin, a hyperbola was rotated around the depth direction axis to generate the cone-like shaped filter, which is written as:

$$\frac{R^2}{a^2} + \frac{z^2}{b^2} = 1 \tag{1}$$

where z is the coordinate of the depth direction, R is the radius of the filter in the cross section of the z axis. a and b represent the shape of the hyperbola. Parameter a and b were set to $a = 2\,\mathrm{m}^{-1}$ and $b = 9\,\mathrm{GHz}$ respectively, according to the inclination of the surfaces in the volume image. To prevent the distortion by strict cut-off, the value of the filter attenuates as it moves away from the depth direction axis. For the attenuation, 2D Hanning window was used, which is defined as follows

$$W(r) = \begin{cases} 0.5 + 0.5\cos\left(\pi \frac{r}{R}\right), & \text{if } 0 \le r \le R, \\ 0, & \text{otherwise.} \end{cases} \tag{2}$$

$$r = \sqrt{x^2 + y^2}. \tag{3}$$

Since the Fourier Transform assumes periodicity, the presence of discontinuities at the edges of the analyzed interval causes Gibbs phenomenon. By inverting the data in the longitudinal and transverse direction before performing the 3D DFT, the connectivity at the boundaries is preserved and the smooth signal is obtained [19]. Volume III of Figure 1 plots the depth at which the local maxima is taken at each point for the filtered data. There are smooth surfaces such as the pavement surface, the pavement-slab boundary surface, and the rebar vertex surface. In some cases, the number of points as a surface was small, or the surfaces were connected to each other in the depth direction. Deletions were made for sets of points that were less than 0.98 times and more than 1.02 times the product of the number of channel points and the number of bridge axis direction data points. The surfaces obtained in this way are used as reference surfaces, and the average of each reference surface in the depth direction is calculated. The signals at each position were resampled so that the depths of the local maxima are consistent with the average depth of each reference surface. An example using two signals acquired at different position is shown in Figure 8. The average depth indices of the surfaces are 236 and 332, respectively, and the interval between the two surfaces is equally divided and resampled so that the red dots match the indices. The number of points between the reference points is the difference of the average depths of the surfaces. In the case of the Figure 8, there are $332-236 = 106$ points. By performing the operations in each interval between the surfaces, we can align the peaks of each signal and remove the trend in the depth direction, as shown in the right figure of Figure 8. In this way, we obtain the detrended volume, which is the same to Volume II in the flow chart Figure 1.

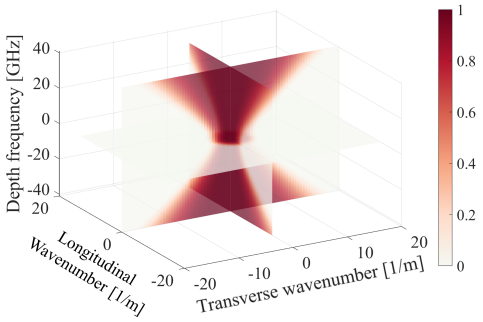

Fig. 7. Surface extraction processing by 3D filtering processing. (a) Cross section of the cone-like shaped filter in the longitudinal and transverse and depth direction. (b) Volume I and extracted surfaces by 3D filtering and local maxima extraction processing. Pavement, boundary of pavement and bridge deck, and rebar mesh surfaces are extracted.

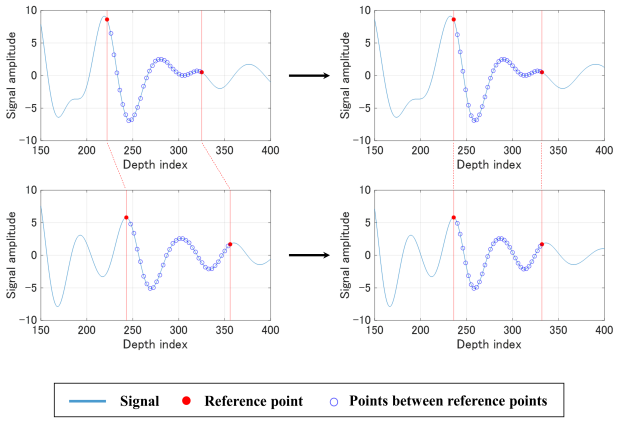

Fig. 8. Conceptual diagrams of detrend processing. The left figures show the signal before processing acquired at two points. The right figures show the signal after appropriate resampling. The reference points are aligned after the processing.

C. Emphasis of Rebar Responses by 3D Filtering

In this section, further noise reduction is done by the filtering that emphasizes rebar responses on Volume II. Depth indices from 251 to 650 (equivalent to $3.06\,\mathrm{ns} \sim 7.93\,\mathrm{ns}$) were taken and interpolated so that there are 512 points in the depth direction and 256 points in the longitudinal and transverse direction for the purpose of using the Fast Fourier Transform algorithm. As in Section II-B, interpolated volume was inverted in the longitudinal and transverse direction and subjected to the 3D DFT. In the wavenumber space, rebar components appear on the longitudinal and the transverse direction axes (Appendix). Extracting only these components on the axes enables to emphasize the rebar responses more. The filter used is shown in Figure 9. It is made by combining two filters; the first one is for extracting the components close to the axes. In general, due to the driving conditions and construction conditions, the longitudinal direction of the vehicle and the direction of the rebar mesh rarely coincide perfectly, and the rebar responses are often seen at a slight angle on the received signal. We tried to extract the rebar responses close to the obtained signals with less distortion by using the filter that attenuates in proportion to the angle from the axes. Normal

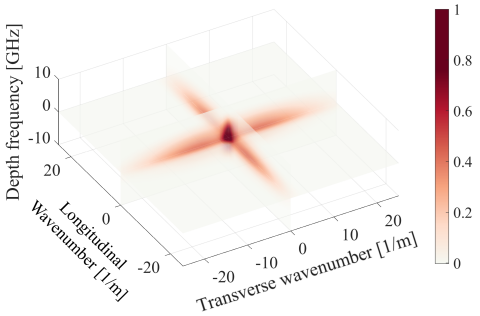

Fig. 9. Sliced image of the 3D rebar emphasizing filter. The filter extracts the components along longitudinal and transverse axes. 3D Hanning window is used to remove high-frequency noise components.

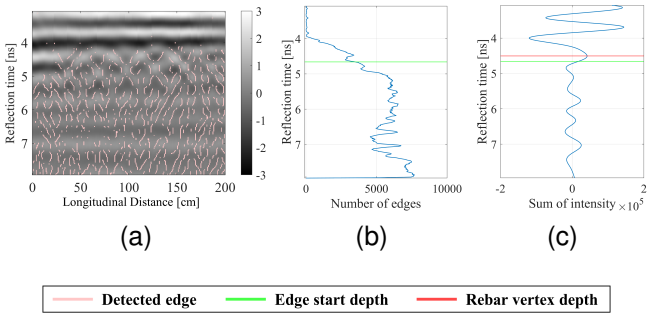

Fig. 10. Process of identifying the surface that includes rebar vertex response. (a) Cross section image of interpolated volume and detected edges from Specimen II. (b) Sum of edges in each depth and detected edge start depth by change point detection algorithm. (c) Sum of intensity in each depth and determined rebar vertex depth.

distribution was adopted for this attenuation. When the angle away from the axis is θ degrees, the attenuation is expressed as follows

$$f(\theta) = \frac{1}{\sqrt{2\pi\sigma^2}} \exp\left(-\frac{\theta^2}{2\sigma^2}\right). \tag{4}$$

The standard deviation σ was set to $3\,\mathrm{degrees}$. When only the angle is used as a variable, the high frequencies are emphasized more than the low frequencies. To suppress this effect, $f(\theta)$ was divided by the distance r from a origin. To avoid division by zero, a constant α was added to the distance

$$f(\theta) = \frac{1}{\sqrt{2\pi\sigma^2}} \exp\left(-\frac{\theta^2}{2\sigma^2}\right) \times \frac{1}{r+\alpha}. \tag{5}$$

On the wavenumber plane, α is set to $3\,\mathrm{m}^{-1}$. Another problem with the above process is that differentiation becomes impossible at $\theta = 45\,\mathrm{degrees}$ and noise is generated after the filter. To address this problem, a 2D Gaussian filter is applied to maintain the overall smoothness. The standard deviation of the Gaussian filter is set to $1\,\mathrm{m}^{-1}$. The 3D filter is constructed by piling the 2D filter up in the depth direction. The second filter is 3D Hanning window that removes high frequency components, which is defined as follows:

$$W(r) = \begin{cases} 0.5 + 0.5\cos(\pi r), & \text{if } 0 \le r \le 1, \\ 0, & \text{otherwise.} \end{cases} \tag{6}$$

$$r = \sqrt{\frac{x^2}{a^2} + \frac{y^2}{b^2} + \frac{z^2}{c^2}} \tag{7}$$

where, a,b,c are the cut-off frequency in each axis. The cut-off frequency in the longitudinal and transverse directions were set to $30\,\mathrm{m}^{-1}$. and in the depth direction to $8\,\mathrm{GHz}$. The rebar emphasized volume, which is called Volume III shown in Figure 1, is obtained by applying the above two filters sequentially to the 3D DFT of the interpolated signal and performing the 3D IDFT.

D. Depth Estimation of Rebar Vertex Responses

For Volume III, at each longitudinal and transverse position, we obtain the points that takes local maxima in the depth direction. One of the surfaces obtained by this operation is the one containing the rebar vertex response (Figure 1). Identifying the rebar vertex surface was achieved by focusing on the complexity of the interference of the hyperbolic responses of the rebars. Because of the interference, multiple diagonal and vertical lines appear below the depth of the rebar vertex in the radar image. Edge detection method was applied to detect these diagonal and vertical lines. For each longitudinal-depth cross section of the interpolated volume, canny edge detection method was applied, which is a method that can capture small edges [20]. To delete the horizontal lines of the detected edge, morphological opening operation was applied [21]. The structuring element used was a line that have length of 2 pixels in vertical direction. The result for Specimen II is shown in Figure 10a, and only diagonal edges are detected in the radar cross section image. After edge detection and morphological operation, the sum of the edges in each depth was calculated. The depth that the number of the detected edges steeply changes is assumed to be near the depth that the rebar vertex response exists. To detect this edge start depth, change point detection [22], [23] was used to find this depth (10b). In this algorithm, a signal is divided at a point and empirical estimates are computed within each section. The deviation from the computed empirical estimate is calculated at each point and summed for each section. The point at which the sum of the residual errors is the smallest is defined as the change point. Mean value was used as the statistic; it minimizes the function below:

$$\begin{aligned} f(k) = &\sum_{i=1}^{k-1} (x_i - \mathrm{mean}(x_1, ..., x_{k-1}))^2 \\ &+ \sum_{i=k}^{N} (x_i - \mathrm{mean}(x_k, ..., x_n))^2 \end{aligned} \tag{8}$$

where, x_i is the target signal, N is the length of the signal and k is the splitting point. For hyperbola becomes steep as it moves away from the vertex, the edge start depth appears deeper than the depth of the rebar vertex depth. Of the index where the sum of intensity of interpolated volume in each depth takes maximal value, the index that is the closest and shallower than the detected change point was determined as rebar vertex depth (Figure 10c). Based on this rebar vertex

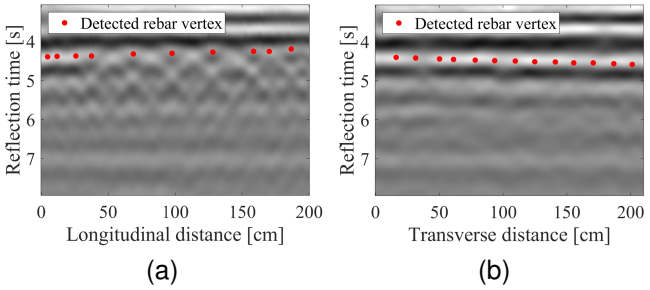

Fig. 11. Cross section of Volume I of Specimen II and locations of the detected rebars. (a) Longitudinal cross section image. (b) Transverse cross section image. The proposed method detected the strong intensity points that is assumed to be corresponding to the rebar vertex response.

depth, the rebar vertex surface can be extracted from local maxima points of Volume III (Figure 1).

E. Rebar Mesh Reproduction

The depth of the rebar vertex surface obtained in the previous section is called the depth map. By obtaining the intensities on Volume III at the points corresponding to the depth map, the intensity map is obtained (Figure 1). The mesh was reproduced by calculating the minimal value of the second-order derivative of the intensity surface in the direction of each longitudinal and transverse axis and overlaying one another. The reason of using second-order derivative instead of directly calculating the local maxima is to emphasize the high wavenumber components corresponding to the rebar spacing and to capture the weak changes. On the other hand, smoothing by a moving average filter is introduced for each derivative to remove the high wavenumber components corresponding to noise above the target wavenumber. Since Volume III has been subjected to 3D trend removal in Section II-B, the depth of the reproduced rebar mesh in the Volume I data is restored by the inverse processing of the trend removal.

Overlaying the detected rebar responses on the cross section of Volume I confirms that only the vertices of the hyperbolas are extracted (Figures 11a, 11b). In addition, 3D drawings are shown in Figures 12a to 12d. The meshes are separated into two directions by morphological opening operation. For the confirmation of the effectiveness of the filter, meshes without the rebar emphasizing filtering processing are shown in Figures 12a and 12b. These meshes were reproduced by focusing directly on the local maxima of the intensity maps, because they contained much noise. Compared to the filtered meshes of Figures 12c and 12d, the meshes without the filtering contain much noise and some rebars are not detected, which shows the effectiveness of the rebar emphasizing filter. Now, it can be noticed that the rebar mesh obtained are locally sinking or undulating in the depth direction. This phenomenon is assumed to be reflecting the local difference in relative permittivity. There is probability that the damages can be detected focusing on the sinking or rising of the rebar mesh in the future study.

Also, we want to note that for Specimen II, when the distribution rebars are located sparsely at interval of 30 cm, the responses by the interference of the hyperbolas were detected

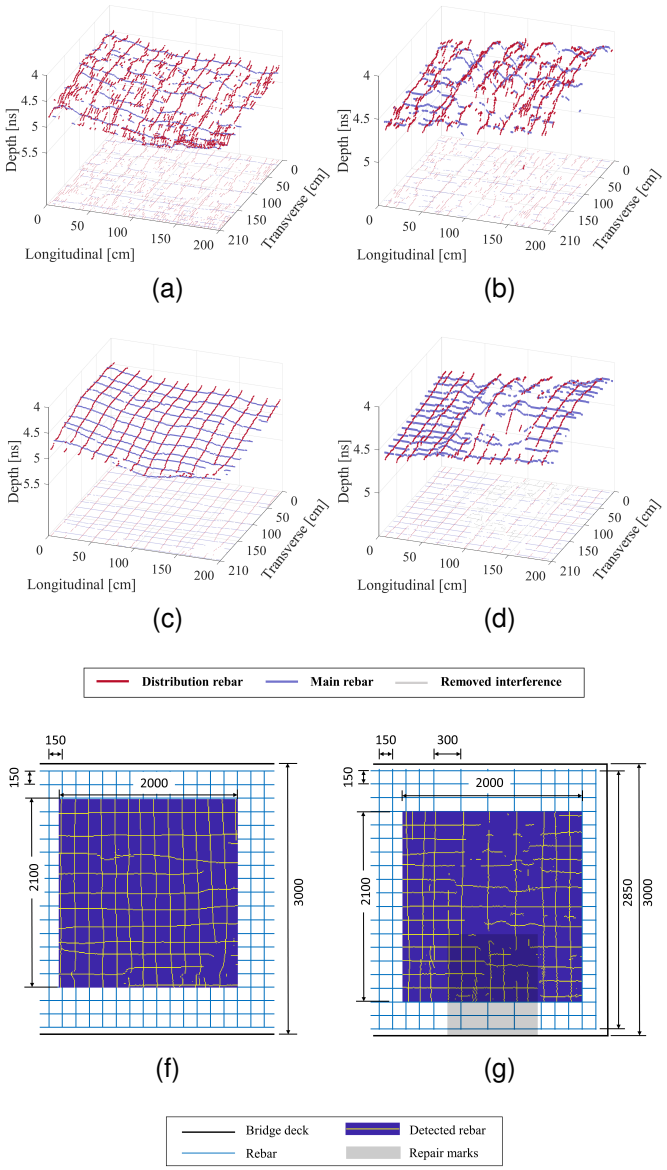

Fig. 12. Results of reproduced rebar mesh. (a)(c)(e) are the results of Specimen I. (b)(d)(f) are the results of Specimen II. (a) and (b) show the mesh reproduced excluding the filtering processing. (c) and (d) show the rebar mesh reproduced by the proposed method. Overall noise is reduced compared to the mesh without the filtering processing. (e) and (f) are the comparison of the meshes with the design drawings of the specimens. Distribution rebars are detected in correct spacing.

as the rebar (Figure 12d, shown in gray lines in horizontal projection). To deal with this problem, we focused on the depth map. Firstly, the maximum value filter is applied to the depth map in a certain direction. Next, the median filter is applied in the same direction for smoothing. In this way, a smooth envelope surface along the depth map is produced. Since the interference response appears deeper than the depth of the rebar vertex response, the intensity was not obtained for points that are further than a certain depth from the envelope surface and were excluded from the mesh reproduction processing. The process successfully removed the interference response (Figure 12d, shown in red and blue lines).

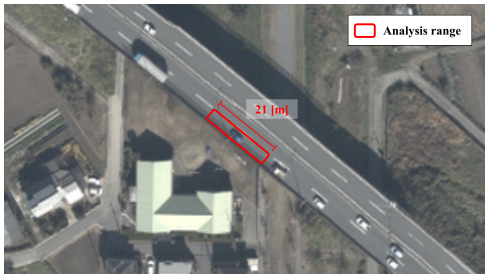

Fig. 13. Location of the analyzed bridge (Saitama-Prefecture, Japan). Red rectangle shows the data acquisition range.

In Figures 12f, 12g, detected meshes and the design drawings of the specimens are overlaid. For the distribution rebar, it is recognized that the detection results match well with the design drawings for both specimens. In the bottom part of Figure 12g, the unwanted lines are caused by the repair marks of the bridge deck in the test field. In the upper part, four intervals are aligned with a spacing of 30 cm that matches with the design drawing image. For the main rebars, left part of Figure 12g shows coincidence with the design drawing, however, there are not less parts that the detection is not going well. The reason for this is assumed to be the remaining of antennas' directivity and frequency characteristics, though clutter removal processing was applied in Section II-A. Also, the fact that hyperbola is flat near the vertex is assumed to be the reason. Although this makes it difficult to estimate the rebar spacing of the bridges, it is certain that this algorithm detects relatively high intensity points which include the information of rebar reflection. Therefore, it can be inferred that the proposed method is sufficient for detecting damages of bridge decks. In the future, to realize the highly accurate spacing estimation, it is required to improve the clutter removal method and to remove the antenna characteristics to the maximum extent.

III. Application to In-Service Bridge Data

The proposed method was applied to data obtained from driving on a bridge under use to confirm its practicality. The data was acquired at a bridge in Saitama-Prefecture, Japan (Figure 13). The number of channels and a spacing of the radar used are 25 and 7.5 [cm], respectively, thus the data can be acquired with a width of 180 cm in the transverse direction. In the longitudinal direction, data is acquired at intervals of 7.0 cm. As pre-processing, bandwidth limitation, zero padding, and clutter removal described in Section II-A were performed. Every 30 points (210 cm) in the driving direction were taken out and analyzed for each section to generate the rebar mesh with the total length of 300 points (21 m). The 3D view and plan view of the generated rebar mesh are shown in Figure 14a. Now, the continuity of the mesh is noteworthy. Although the mesh is divided into 10 sections, the depth directional connections are maintained at the boundaries, indicating that the distortion caused by the filter is minimized.

Also, to confirm the stability among the analysis section, spacing of the distribution rebar was calculated in each section using the 1D DFT. The meshes obtained were converted to the

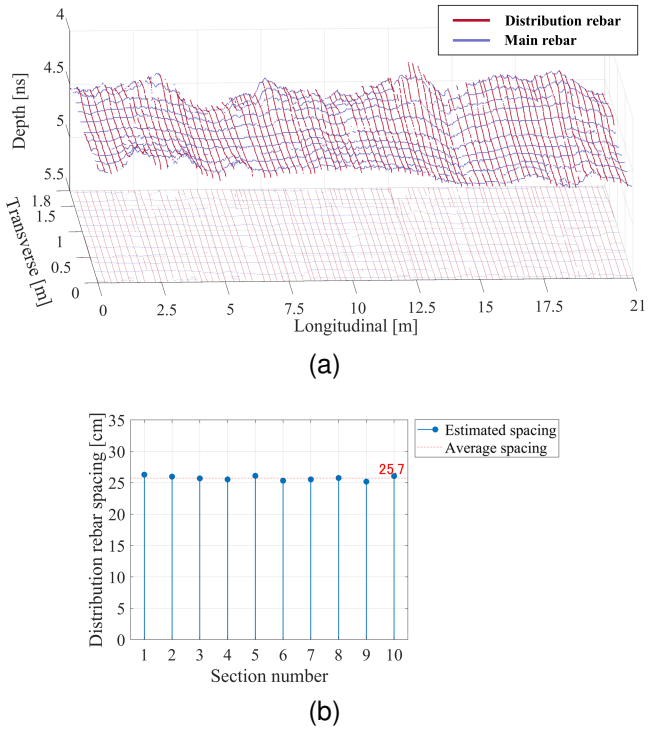

Fig. 14. Results of applying the proposed method to the in-service bridge data. (a) Reproduced rebar mesh and the projection of the mesh. The smoothness of the mesh at the boundary of analysis sections is noteworthy. (b) Calculated distribution rebar spacing. Stable reproduction is achieved.

binary data, and rebars distribution rebars were extracted by morphological opening operation. Then, Gaussian filter was applied to make the signal smooth and to remove the harmonic components. After that, 1D DFT in each direction was applied. In general, the rebars of bridge decks must be installed with a spacing of 10 cm to 30 cm [24], thus the wavenumber that takes maximum value in this range was determined to be the rebar spacing. The average of the calculated wavenumber of all the rows is determined to be the distribution rebar spacing in that section. The result is shown in Figure 14b. We can notice less variance among the analysis section, which means that the reproduction of mesh is carried out stably. It can be concluded that the proposed method effectively and stably functions for the in-service bridge data.

IV. Discussion and Conclusion

In this study, the automated algorithm to extract rebar vertex responses in radar volume images of bridge decks acquired by an on-vehicle air-coupled GPR was proposed. In Section II, measurements using bridge deck specimens were done to establish the method. Firstly, trend removal of the volume images was done based on the surface extraction by the 3D filtering method. Then, another 3D filtering was done to extract the rebar mesh components that appears around the longitudinal/transverse direction axes in the frequency domain. The surface containing the rebar vertex response was identified by applying edge detection and change point detection focusing on the interference of the hyperbolic responses. The rebar mesh was reproduced by extracting the minimal values of the

second-order derivative in the signal intensity on the surface in both longitudinal and transverse direction. By adding the removed trend, the mesh was restored to the original depth. We could confirm that the cross section of the radar image and the detected vertex coincided. Also, for the distribution rebar, the reproduced mesh and the design drawing of the specimens matched accurately. For the main rebar, there were some parts that the reproduction in real spacing was not well achieved. However, it is sufficient for detecting damages of bridge decks because it is assumed that proposed algorithm detects relatively high intensity points which include the information of rebar reflection. Therefore, for precise estimation of the main rebars, improvements in the clutter removal method and the antenna characteristics are desired. In Section III, the radar data of the bridge in service was obtained and analyzed by the proposed method. The data was 21 m long and was divided into 10 sections. It was found that the depth at the boundary of the analysis section was maintained, which shows that the rebar was captured with small distortion due to filtering. Also, the calculated distribution rebar spacing was stable among the analysis sections. From these point of views, in conclusion, the proposed method effectively functions for the in-service bridge data. In the future study, we expect the development of automatic detection of damage of bridge decks, such as concrete sedimentation and crack detection, focusing on the intensity features around the rebar responses.

APPENDIX

THE 3D DFT OF IDEAL REBAR MESH

This appendix shows the results of the 3D DFT of ideal rebar mesh based on the projection theorem. The 3D Fourier Transform can be defined as natural extension of the 1D Fourier Transform, which is written as follows:

$$F(u,v,w) = \iiint f(x,y,z)e^{-2\pi(ux+vy+wz)}dxdydz \quad (9)$$

where, (x,y,z) are the coordinates of the time domain, and (u,v,w) are the coordinates of the frequency domain. Simultaneously, we consider projection of $f(x,y,z)$ to a straight line. Let t be the coordinate along the axis of this line, projection can be written as:

$$P(\theta,\phi,t) = \iiint f(x,y,z) \delta(x\sin\theta\cos\phi + y\sin\theta\sin\phi + z\cos\theta - t)dxdydz \quad (10)$$

where, δ is Dirac delta function and (θ,ϕ) are the angles of the polar coordinates. This operation is known as Radon transform. Now, we consider the Fourier Transform of the projection $P(\theta,\phi,t)$. When the frequency along the straight projection line is ω, the Fourier Transform $S(\theta,\phi,\omega)$is

$$S(\theta,\phi,\omega) = \iiint f(x,y,z) \delta(x\sin\theta\cos\phi + y\sin\theta\sin\phi + z\cos\theta - t)dxdydze^{-i2\pi\omega t}dt. \quad (11)$$

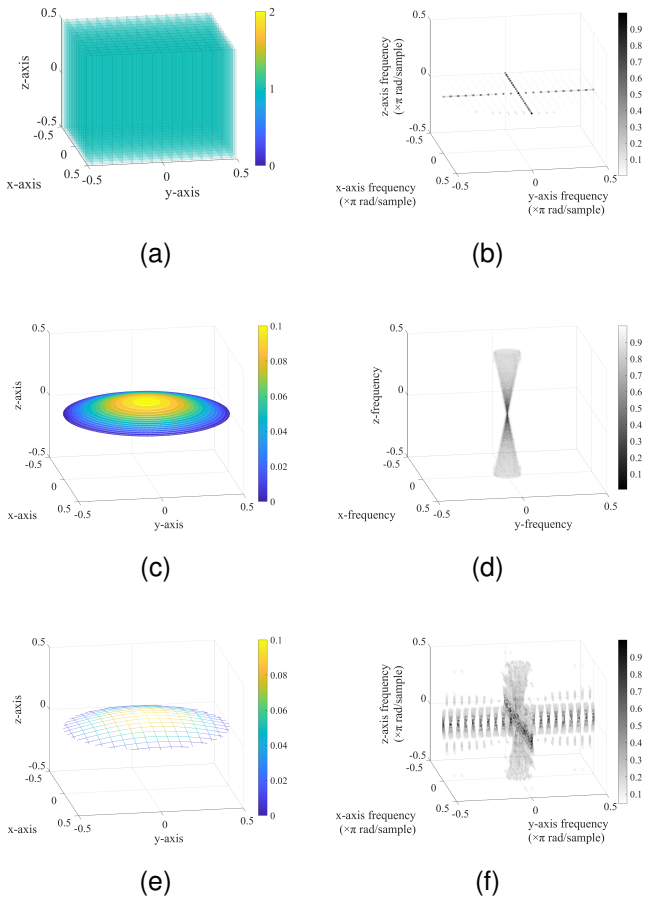

Fig. 15. The results of applying the 3D DFT to the ideal mesh and surface volume images. (a)(c)(e) show the volumes in the time domain. (b)(d)(e) show the results of applying the 3D FFT to the data.

When we calculate the integral of t first, the equation will be:

$$S(\theta,\phi,\omega) = \iiint f(x,y,z) e^{-i2\pi\omega(x\sin\theta\cos\phi + y\sin\theta\sin\phi + z\cos\theta)}dxdydz = F(\omega\sin\theta\cos\phi, \omega\sin\theta\sin\phi, \omega\cos\theta) \quad (12)$$

which means that the 1D Fourier Transform of the projection $S(\theta,\phi,\omega)$ is equal to the components along the straight line of the 3D Fourier Transform of the volume $F(u,v,w)$. When the 3D Fourier Transform is applied to a plane that has constant values only on $x\sin\theta\cos\phi + y\sin\theta\sin\phi + z\cos\theta = 0$, the values appear on a line in the direction that corresponds to the normal vector of the plane in the frequency domain. This is called the projection theorem.

For discrete time system, the 3D DFT can be applied as follows:

$$F(u,v,w) = \sum_{x=0}^{N_1-1}\sum_{y=0}^{N_2-1}\sum_{z=0}^{N_3-1} f(x,y,z)e^{-i2\pi\left(\frac{ux}{N_1}+\frac{vy}{N_2}+\frac{wz}{N_3}\right)} \quad (13)$$

where, (x, y, z) are the coordinates of the time domain, and (u, v, w) are the coordinates of the frequency domain. N_1,N_2,N_3 refers to the length of the volume in each axis. As the 3D DFT of curved mesh shape being difficult to be solved analytically, numerical simulation was done. Firstly, a volume that has the same meshed-shape cross section in the z-axis direction is considered (Figure 15a). Each side of the volume has 301 samples and the mesh spacing is set to 20 samples. Amplitudes of the 3D DFT of this volume show the shape shown in Figure 15b that has a value only on a plane of $z = 0$. This is because, after adopting the 1D DFT to x-axis, then y-axis of the volume, it has constant values in z-axis. Therefore, the 1D DFT in z-axis direction has only DC component. Simultaneously, a curved surface expressed by rotating the sinusoidal curve around the z-axis is considered here, which can be written as follows

$$f(x, y) = \alpha \cos \pi \sqrt{x^2 + y^2} \quad (-\frac{1}{2} \leq \sqrt{x^2 + y^2} \leq \frac{1}{2}). \quad (14)$$

Figure 15c and 15d show the surface and the result of the 3D DFT when $\alpha = 0.1$. Based on the projection theorem, the intensity of the components along the direction of normal vector of the surface at $\sqrt{x^2 + y^2} = 1/2$ is relatively strong, thus cone-like spectrum appears. When the cone shaped filter is adopted to the 3D spectrum of the volume, surfaces that have the specific gradient range can be extracted.

An ideal curved mesh was generated by calculating the product of the mesh volume and the curved surface. The mesh and the result of the 3D DFT are shown in Figure 15e, 15f. Convolution theorem is valid for the 3D DFT, and it can be noticed that the spectrum of the curved mesh is expressed as convolution of the two previous spectrums. Removing the radar volume's trend in Section II-C has a role of concentrating the components on x-axis and y-axis in the wavenumber domain. Furthermore, extracting the components only on x-axis and y-axis can emphasize the rebar responses in the volume.

REFERENCES

[1] Infrastructure, Transp. and Tourism, Japan Ministry of Land. Infrastructure maintenance information (in japanese). Accessed: Aug. 1, 2022. [Online]. Available: https://www.mlit.go.jp/sogoseisaku/maintenance/02research/02_01_01.html

[2] T. Yamaguchi, T. Mizutani, and T. Nagayama, "Mapping subsurface utility pipes by 3-d convolutional neural network and kirchhoff migration using gpr images," *IEEE Trans. on Geosci. and Remote Sens.*, vol. 59, no. 8, pp. 6525–6536, 2021.

[3] T. Yamaguchi, T. Mizutani, M. Kimiro, and T. Hirano, "Detecting subsurface voids from gpr images by 3-d convolutional neural network using 2-d finite difference time domain method," *IEEE J. of Sel. Topics in Appl. Earth Observ. and Remote Sens.*, 2022.

[4] P. Gamba and S. Lossani, "Neural detection of pipe signatures in ground penetrating radar images," *IEEE Trans. on Geosci. and Remote Sens.*, vol. 38, pp. 790–797, 2000.

[5] E. Pettinelli, A. Di Matteo, E. Mattei, L. Crocco, F. Soldovieri, J. D. Redman, and A. P. Annan, "Gpr response from buried pipes: Measurement on field site and tomographic reconstructions," *IEEE Trans. on Geosci. and Remote Sens.*, vol. 47, no. 8, pp. 2639–2645, 2009.

[6] T. Mizutani, N. Nakamura, T. Yamaguchi, M. Tarumi, Y. Ando, and I. Hara, "Bridge slab damage detection by signal processing of uhf-band ground penetrating radar data," *J. of Disaster Res.*, vol. 12, no. 3, pp. 415–421, 2017.

[7] Z. W. Wang, M. Zhou, G. G. Slabaugh, J. Zhai, and T. Fang, "Automatic detection of bridge deck condition from ground penetrating radar images," *IEEE Trans. on Automat. Sci. and Eng.*, vol. 8, pp. 633–640, Jul. 2011.

[8] M. Abouhamad, T. Dawood, A. Jabri, M. Alsharqawi, and T. Zayed, "Corrosiveness mapping of bridge decks using image-based analysis of gpr data," *Automation in Construction*, vol. 80, pp. 104–117, Aug. 2017.

[9] U. Pe'er and J. G. Dy, "Automated target detection for geophysical applications," *IEEE Trans. on Geosci. and Remote Sens.*, vol. 55, no. 3, pp. 1563–1572, 2017.

[10] P. Asadi, M. Gindy, and M. Alvarez, "A machine learning based approach for automatic rebar detection and quantification of deterioration in concrete bridge deck ground penetrating radar b-scan images," *KSCE J. of Civil Eng.*, 2019.

[11] X. Ma, H. Liu, M. L. Wang, and R. Birken, "Automatic detection of steel rebar in bridge decks from ground penetrating radar data," *J. of Appl. Geophys.*, vol. 158, pp. 93–102, Nov. 2018.

[12] K. Dinh, N. Gucunski, and T. H. Duong, "An algorithm for automatic localization and detection of rebars from gpr data of concrete bridge decks," *Automat. in Construction*, vol. 89, pp. 292–298, May. 2018.

[13] H. Liu, C. Lin, J. Cui, L. Fan, X. Xie, and B. F. Spencer, "Detection and localization of rebar in concrete by deep learning using ground penetrating radar," *Automat. in Construction*, vol. 118, Oct. 2020.

[14] R. Persico, *Introduction to Ground Penetrating Radar*. Piscataway, NJ, USA: IEEE Press, 2014.

[15] D. J. Daniels, *Ground Penetrating Radar*. The Institution of Eng. and Technol., 2004.

[16] A. Benedetto, F. Tosti, L. B. Ciampoli, and F. D'Amico, "An overview of ground-penetrating radar signal processing techniques for road inspections," *Signal Processing*, vol. 132, pp. 201–209, Mar. 2017.

[17] D. R. Wehner, *High-resolution Radar*. Norwood, MA, USA: Artech House, 1995.

[18] D. C. Nobes, "Geophysical surveys of burial sites: A case study of the oaro urupa," *Geophysics*, vol. 64, no. 2, pp. 357–367, 1999, accessed: Aug. 1, 2022. [Online]. Available: https://doi.org/10.1190/1.1444540

[19] S. Mallat, *A Wavelet Tour of Signal Processing, Third Edition: The Sparse Way*, 3rd ed. USA: New York, NY, USA; Orlando, FL, USA; San Diego, CA, USA: Academic, 2008.

[20] J. Canny, "A computational approach to edge detection," *IEEE Trans. on Pattern Anal. and Machine Intelligence*, vol. PAMI-8, pp. 679–698, 1986.

[21] A. Bovik, *Handbook of Image and Video Processing*, ser. Academic Press series in communications, Netw. and multimedia. New York, NY, USA; Orlando, FL, USA; San Diego, CA, USA: Academic, 2000.

[22] MathWorks. Find abrupt changes in signal. Accessed: Aug. 1, 2022. [Online]. Available: https://jp.mathworks.com/help/signal/ref/findchangepts.html?lang=en

[23] M. Lavielle, "Using penalized contrasts for the change-point problem," *Signal Processing*, vol. 85, no. 8, pp. 1501–1510, 2005, accessed: Aug. 1, 2022. [Online]. Available: https://www.sciencedirect.com/science/article/pii/S0165168405000381

[24] Japan Road Association, *Specifications for Highway Bridges*. Japan Road Association, 2017.

Tsukasa Mizutani Tsukasa Mizutani (Member, IEEE) was born in Osaka, Japan, in 1983. He received the B.S. degree in urban engineering, and the M.S. and Ph.D. degrees in civil engineering from the University of Tokyo, Tokyo, Japan, in 2007, 2009, and 2011, respectively. He was an Assistant Professor with the Department of Civil Engineering, School of Engineering, the University of Tokyo, from 2011 to 2017. He was a Project Lecturer with the Institute of Industrial Science (IIS), the University of Tokyo, from 2017 to 2019, and has been an Associate Professor with IIS since 2019. His research interests include digital signal processing, and electromagnetic wave measurement for structural health monitoring. Dr. Mizutani was the recipient of the 2020 ASCE Moisseiff Award, and the 2020 Prize for Science and Technology (Young Scientist Category), the Commendation for Science and Technology by the Minister of Education, Culture, Sports, Science, and Technology in Japan.

Takanori Imai Takanori Imai was born in Fukuoka, Japan, in 1999. He received the B.S degree in civil engineering from the University of Tokyo in 2022. He is a master course student in civil engineering from the Graduate School, the University of Tokyo. He is also selected as a student of World-leading Innovative Graduate Study Program Co-designing Future Society (WINGS-CFS), the University of Tokyo. His research interests include digital signal processing and super resolution of ground penetrating radar images.